Production of Sub-Micron Flakes of UPt$_3$ for the Study of a New 2D Material

Eli Martel

Master of Science

Department of Physics
McGill University
Montréal, Québec, Canada

July 2019

Under the supervision of Guillaume Gervais and Thomas Szkopek

A thesis submitted to McGill University in partial fulfillment of the requirements of the degree of Master of Science.

Abstract

The bulk (3D) properties of UPt_3 have been well documented and understood for the past few decades, besides the exact nature of its superconductivity. It is known to be a heavy fermion metal which exhibits both antiferromagnetic ordering and superconductivity under certain conditions, making it an unconventional superconductor. Its superconducting pairs have non-zero angular momentum, making it potentially topologically non-trivial. Theoretical studies therefore predict the presence of Majorana fermions in the form of zero energy modes. However, nothing is known about its behavior when electronic confinement approaches the 2D regime, and if strong spin-orbit coupling could lead to a chiral Fermi liquid normal state.

Flakes of micrometer and sub-micrometer thicknesses obtained through micromechanical fracturing were studied using optical microscopy, atomic force microscopy and scanning electron microscopy, as well as Raman spectroscopy, where the peak in the Stokes shift at $80\,\mathrm{cm}^{-1}$ was observed for bulk samples at room temperature. Electron beam lithography was employed in order to fabricate devices with these flakes, where 100 nm Ni/Au contacts were deposited using electron beam evaporation, however the uneven surface of the flakes prevented proper van der Waals adhesion to the substrate, making it impossible to study any of the flakes before coming off. We propose alternative methods for obtaining 2D flakes, as well as certain experimental details to determine the nature of UPt_3 once such thin flakes can be achieved.

Abrégé

Les propriétés volumiques (3D) de UPt_3 sont bien documentées et comprises depuis quelques décennies, mise à part de la nature exacte de sa supraconductivité. C'est reconnu comme étant un métal à fermions lourds et qui présente à la fois des propriétés antiferromagnétiques et la supraconductivité sous certaines conditions, ce qui en fait de celui-ci un supraconducteur non-conventionnel. Ses paires supraconductrices ont un moment angulaire non-nul, ce qui le rend potentiellement topologiquement non-trivial. Selon la théorie, des fermions de Majorana sont prédits dans ce système sous la forme d'états de zéro énergie. Cependant, on ne sait rien de son comportement lorsque le confinement électronique s'approche du régime 2D, et si un couplage spin-orbit élevé puisse mener à une nouvelle sorte de liquide de Fermi, dite *chiral*, dans son état normal.

Des flocons de UPt_3 obtenus suite à une fracturation micro-mécanique, mesurant environ un micron et moins en épaisseur, ont été étudié grâce à la microscopie optique, la microscopie à force atomique et la microscopie électronique à balayage, ainsi que par la spectroscopie de Raman où le pic de Stokes à $80\,\mathrm{cm}^{-1}$ a été observé pour un échantillon macroscopique. La lithographie à faisceau d'électrons a été employé afin de fabriquer des dispositifs avec ces flocons, sur lesquels des contacts de $100\,\mathrm{nm}$ de Ni/Au étaient déposés avec un évaporateur à faisceau d'électrons.

Acknowledgements

My most sincere thanks go out to Guillaume Gervais for taunting me with the opportunity to work with such an exotic material as UPt_3, as well as entrusting me with such a great project and set of challenges.

My gratitude extends to Thomas Szkopek who graciously let me work in his lab with his crew, and who provided me with powerful insight and teachings in all matters pertaining to electronics. Thank you for listening to my many, many issues with fabrication and giving me clear explanations and answers to Guillaume's crazier ideas.

Many thanks go out to William P. Halperin at Northwestern University for providing us with some of his precious UPt_3 crystals. Without it, none of this adventure could have taken place.

Without a doubt, I must thank Marie-Hélène Bernier at Polytechnique for being immensely kind and helpful, devoting much of her own time to explain things over and over.

Finally I must thank both of my teams, for all of your support and aid in the laboratory. Specifically, I'd like to thank Oulin Yu for helping me deal with far too many difficulties with the EBL systems, and many other hurdles I've had to leap over, Ibrahim Fakih and Nicholas Hemsworth for dealing with my incessant questions as a newcomer to the lab, which persist even to this day, Fatma Oudjedi for using her knowledge and kindness to find the time and patience to help me with various apparatuses, Melis Aygar for revolutionizing the way we approach EBL designs and fabrication, Marwan Chehad for being my only companion

on weekends, late nights and early mornings in the lab, Minh Tran for pushing me to get even thinner flakes and entertaining me when I needed it, Pierre-François Duc for helping our lab function properly and providing us all with your vast repertoire of programming excellence, Matei Petrescu for teaching me about ultra-low temperature physics, and Talia Martz-Oberlander for her great support during the lab's darkest hours.

Contributions

I was responsible for the work presented in this thesis for making devices from UPt_3. The original idea was proposed by both Prof. Guillaume Gervais and Prof. Thomas Szkopek.

I was therefore responsible for all of the fabrication work required, such as the mechanical cleaving of bulk samples in order to obtain small flakes of the material, cleanroom processes such as spin-coating resist layers on the substrate and lift-off, as well as electron beam lithography to design contacts for the device and metal deposition to make the metallic contacts. I performed all of the microscopy analysis using optical microscopy, atomic force microscopy and scanning electron microscopy to study the flakes of the material and the devices fabricated afterwards. Raman spectroscopy was performed with the assistance of Léonard Schue (Ph.D.) at Polytechnique Montréal to analyze the smallest flakes and a bulk sample of our material; this is the only exceptional case where another student was involved in the experimental work. I then tested devices and bulk samples in the probe station to characterize their electronic transport properties.

Contents

Chapter 1

Introduction

Since the early 2000s when Geim and Novoselov achieved atomic layer thickness samples of graphene through mechanical exfoliation [1], the field of 2D materials has greatly expanded. The discovery of other 2D materials such as black phophorus in the form of phosphorene has led to the development of field-effect transistors fabricated with these near-atomically thin materials, demonstrating the confinement of charge carriers to two dimensions without necessarily reaching a 2D crystal lattice [2]. As such, it has been shown that 2D variants of materials are not required to follow the same properties as their 3D couterparts, allowing for the study of novel physical phenomena from materials once thought to be fully understood. This has henceforth given us reason to study a material that is still not fully understood even in its usual 3D form; UPt_3.

In this thesis, I will discuss my attempts to exfoliate the topological superconductor UPt_3, with the goal to obtain nanometer-thick flakes in order to characterize UPt_3 in the 2D regime. I will begin by introducing some of the theoretical concepts and models necessary to comprehend the unusual behavior of this material, as well as the many facets of experimental research performed over the last three decades leading to our current understanding of UPt_3 as a heavy fermion compound with unconventional superconductivity. Following this, I will define the methods and tools used to fracture a bulk crystal into smaller fragments, or flakes, and potentially fabricate a device out of the flakes produced during the fracturing process. Finally, the methods needed to characterize the flakes and the devices will be explained, ranging from initial microscopy imaging of flakes to the electrical conductivity measurements used to find the electrical properties of the material.

Chapter 2

Background

UPt_3 is a heavy-fermion compound that was discovered to be superconducting at temperatures of roughly 0.5 K in the early 1980s [3]. Before reaching the critical temperature for superconductivity, UPt_3 becomes antiferromagnetic at a Néel temperature of 5 K, making this the first coexistent superconductor—spin-fluctuation system. However, what makes this compound of particular interest is the discovery that UPt_3 is characterized by several superconducting phases.

In this chapter, the crystal structure, Fermi liquid characteristics, transport properties and unconventional superconducting nature will be further explained so as to convey the intricacies of what makes UPt_3 a material of interest for many applications and theoretical models.

2.1 Crystal Structure

The crystal structure and symmetries of a material are among the most crucial aspects of resolving the nature of transport phenomena within the confines of the solid. The simple arrangement of atoms or molecules dictates the allowed energies of electrons spread throughout the material, as well as the representation of angular momenta associated with the superconducting gap function. More intuitively, the crystal structure can hint at potential anisotropies in charge or heat transport, should there be any asymmetry in the actual layout of the crystal in real space.

UPt$_3$ has hexagonal symmetry, where the uranium atoms follow a hexagonal close-packed structure, and the platinum atoms are located between the in-plane uranium atoms. It is also common to refer to the crystal structure according to the symmetry group that represents the transformations that leave the structure unchanged. UPt$_3$ belongs to the point group D_{6h}, since it exhibits hexagonal symmetry in plane and a vertical inversion symmetry. Research has shown that the symmetry may actually be trigonal, or rather that it may experience slight trigonal distortion, possibly due to stacking faults [4,5,6]. For most calculations, the trigonal distortion is considered to be negligible, leaving only the hexagonal close packed crystal structure. The interlayer spacing is approximately 4.13 Å [4,7], with the a-axis parallel to the ΓK-axis and the b-axis parallel to the ΓM-axis. Incidentally, the c-axis is perpendicular to both of these, forming a complete first 3D Brillouin zone. The principle crystalline axes are illustrated in figure 2.1, as is the crystal structure.

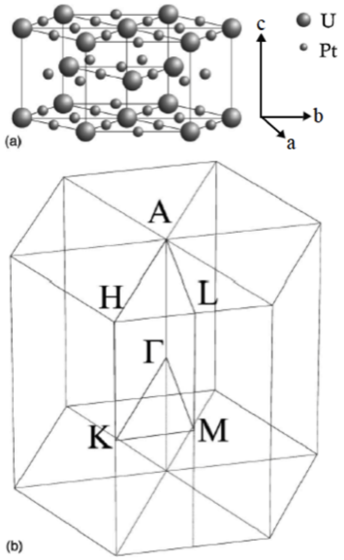

Figure 2.1: a) Illustration of the crystal structure of UPt$_3$ and b) its first Brillouin zone [4].

2.2 Charge and Heat Transport Properties

Typically in a metal, the transport of charge is described as the relation between an applied electric field $\vec{E}$ and the current density obtained $\vec{j}$, such that

$$\vec{E} = \rho\vec{j}. \tag{2.1}$$

The relation is governed by the resistivity ρ of the material, which is the inverse of conductivity, $\sigma = \rho^{-1}$. The resistance of a material vaguely corresponds to the scattering of charge carriers as they are carried across the solid by the external field, which may include elastic and inelastic collisions. Since these kinds of collisions usually occur with the atoms of the solid in question, whose layout may vary in each of the spatial dimensions, it is convenient to re-write the resistivity as a tensor, such that

$$\vec{E} = \hat{\rho}\vec{j}, \tag{2.2}$$

where

$$\hat{\rho} = \begin{bmatrix} \rho_{xx} & \rho_{xy} & \rho_{xz} \\ \rho_{yx} & \rho_{yy} & \rho_{yz} \\ \rho_{zx} & \rho_{zy} & \rho_{zz} \end{bmatrix}.$$

This format reconciles many oversights that may ensue when treating phenomena where the current is not necessarily parallel to the applied electric field. This occurs in a number of situations; for example with the addition of an external magnetic field perpendicular to the electric field. In such cases, terms like ρ_{xy} become non-zero and provide insight into interesting phenomena such as Shubnikov de Haas (SdH) oscillations, defined as the periodic modulation of the resistivity for increasing magnetic field, or the de Haas-van Alphen (dHvA) effect where the magnetization is periodic with increasing magnetic field.

Analogous to the transport of charge related to the electrical conductivity in a material, heat transport can be related to a thermal conductivity defined by Fourier's law,

$$\vec{q} = -k\overrightarrow{\nabla T}, \tag{2.3}$$

where $\vec{q}$ is the heat flux, k is the thermal conductivity and $\overrightarrow{\nabla T}$ is the temperature gradient across the system. Re-writing equation (2.1) with $\vec{E}$ being the gradient of a potential $\overrightarrow{\nabla V}$ one obtains

$$\vec{j} = -\sigma\overrightarrow{\nabla V}$$

making the parallel between both types of transport inevitable. The anisotropy of both heat and charge transport has been observed in experiments, with transport always greater along the direction of the c-axis; for temperatures below 1 K, the ratio for electrical conductivity is $\sigma_c/\sigma_b \approx 2.6$ whereas the thermal conductivity ratio is $\kappa_c/\kappa_b \approx 2.7$ [4,8].

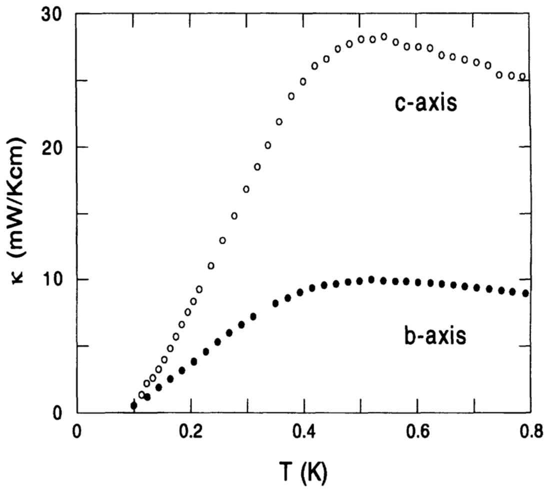

Figure 2.2: Thermal conductivity for heat current along the b-axis and c-axis [8].

Interestingly, below this 1 K low-temperature regime, the conduction ratio is practically independent of temperature, and this anisotropy is the same for the elastic and inelastic terms [9]. One may therefore conclude that all scattering is purely s-wave, meaning it is isotropic in momentum space, and that the anisotropy comes from that of the velocities of the conduction electrons themselves, where $\langle v_c^2 \rangle / \langle v_b^2 \rangle \approx 2.1$ [10].

Since charge carriers in materials are normally fermions, they obey Fermi statistics and therefore, while filling available states in a system, the energies of the fermions increase, until all of the available states are occupied. The highest energy level corresponds to the Fermi energy of the system,

$$E_F = \frac{\hbar^2}{2m} \left(\frac{3\pi^2 N}{V} \right), \tag{2.4}$$

where $\hbar$ corresponds to the reduced Planck constant, m is the mass of the fermion, and N and V are the number of fermions and the volume of the system, respectively. This Fermi energy defines a volume in a 3D space of the filled states of the system, where the surface is known as the Fermi surface, hosting the conducting fermions that therefore carry the charge as a non-interacting gas. Consequently, fermions at the Fermi surface have kinetic energy equal to the Fermi energy, granting them velocities equal to $v_F = \sqrt{\frac{2E_F}{m}}$, hence denoted as the Fermi velocity.

However, UPt_3 like many other real systems plays host to a vastly different type of Fermi surface, where the electrons are highly correlated due to their high density in the solid. Such systems are characterized by an effective mass m^*, portraying the mass the particles would appear to have when responding to external forces, such as that induced by an external magnetic field. Particles of this nature are referred to as quasiparticles, as they are excitations due to many-body correlation effects, and in the case where the effective mass is larger than the electron's rest mass, such quasiparticles are simply called heavy fermions, or heavy quasiparticles. Incidentally, this picture of an interacting Fermi gas is usually referred to as a Fermi liquid, where most of the properties remain the same, albeit some small changes need to be made to keep the underlying framework intact.

Furthermore, charged particles in a magnetic field B undergo cyclotron motion, where the frequency is given as

$$\omega = \frac{qB}{m^*}, \tag{2.5}$$

and where q is the charge of the quasiparticle. As the trajectories of the quasiparticles are modulated by the external magnetic field, the effect known as the de Haas-van Alphen effect takes place. The dHvA effect shows a variation in magnetization that is periodic with increasing magnetic field. The trajectory of a quasiparticle around the 3D Fermi surface, according to the orientation and strength of the magnetic field, gives some valuable insight into the nature of both the quasiparticles of the system and the shape of the Fermi surface. The area A enclosed by the orbit around the Fermi surface, according to the frequency of the varying magnetization $f(\vec{M})$, is given by

$$A = \left(\frac{2\pi q}{\hbar c}\right) f(\vec{M}), \tag{2.6}$$

with c the speed of light. This is known as the Onsager relation, which establishes a concrete way of determining the geometry of the Fermi surface. Using the appropriate area of the orbit, one may also obtain the effective mass of the quasiparticle as

$$m^* = \frac{\hbar^2}{2\pi}\left[\frac{\partial A}{\partial \epsilon}\right]_{\epsilon_F} \approx \frac{\hbar}{v_0}\sqrt{\frac{A}{\pi}}. \tag{2.7}$$

Here, v_0 is the average velocity close to the Fermi velocity of the quasiparticle.

The existence of heavy quasiparticles in UPt_3 was explained due to the particular charge transport properties as well as the direct observation of quantum oscillations through the dHvA effect [3, 11, 12]. Measurements using the dHvA technique have provided effective masses up to roughly 100 m_e, the largest values ever measured at the time. In fact, all the measured effective masses represent very large values when compared to those of an ordinary metal.

By measuring the dHvA frequencies for different orientations of the magnetic field along the crystal axes, a basic representation of the Fermi surface could be made. Figure 2.3 shows the results obtained for such measurements [12].

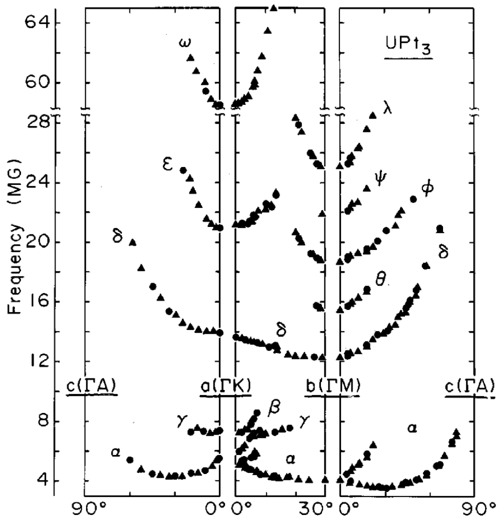

Figure 2.3: Measured de Haas-van Alphen frequencies for different angles of the applied magnetic field according to the crystallographic axes [12].

Theoretical models have been established to further study the actual Fermi surface, mostly by making certain approximations such as all electrons being itinerant and included in the Fermi surface [13]. The surface therefore consists of five separate bands crossing the Fermi level, all with strong f character, giving rise to five (or six) Fermi surface sheets. A model of a simulated Fermi surface is illustrated in figure 2.4.

Most of the dHvA frequencies correspond to the calculated Fermi surface band structure. For example, the structure for a magnetic field parallel to the b-axis and the GM-axis, composed of five equally spaced frequencies δ, θ, ϕ, ψ, and λ (see figure 2.3, is naturally explained in terms of a magnetic breakdown between two orbits centered on point A, respec-

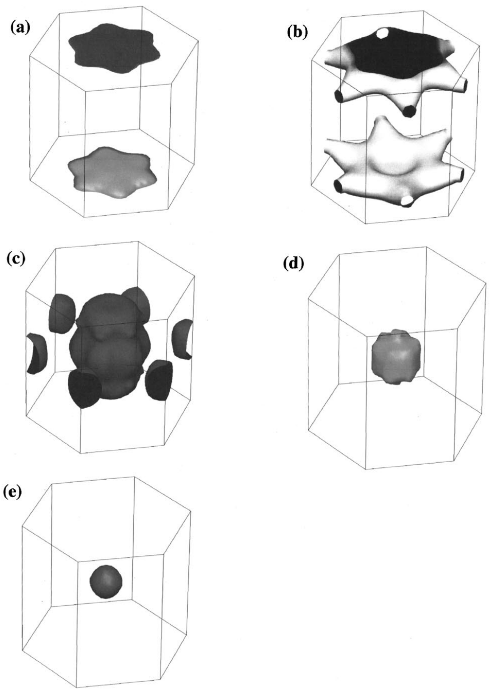

Figure 2.4: Calculated Fermi surfaces where the 5f electrons are assumed to be included in the Fermi volume [13]. These surfaces are noted as a) the "Starfish", b) the "Octopus", c) the "Oyster" surrounded by six "Urchins", d) the "Mussel" and e) the "Pearl". Both the Starfish and Octopus are centered on A, the Oyster is centered on Γ, the Urchins are all centered on K points and both the Mussel and Pearl are centered on Γ as well.

tively supported by the "Starfish" (δ orbit) and the "belly" of the "Octopus" (λ orbit).

Although later experiments found other frequencies which were not observed in the theoretical models [14], further theoretical analysis has managed to take into account these findings and potentially explain the missing Fermi surface sheets using the fully itinerant approach [6]. It therefore remains that the Fermi surface of UPt_3 is still very much as shown in figure 2.4. Not only that, but based on the band structure calculations and previous data, one may consider all three U 5f electrons to be fully delocalized.

One of the greatest sources of debate and confusion over UPt_3 is the nature of the U 5f electrons, that is whether they are localized, partially localized or itinerant. Most data seems to favor an itinerant electron model, that is to say the electrons are spread throughout the solid, forming the interacting electron gas. High resolution angular-resolved photoemission spectroscopy (HR ARPES) data is in good agreement with the dHvA results, favoring the itinerant model [11, 12,15]. The U 5f and Pt 5d bands appear to be well separated in the band structure, the former being located around E_F and the latter being at higher binding energies.

Moreover, this Fermi liquid state breaks down at the Néel temperature of approximately 5 K, when antiferromagnetism sets in. Analogous to the Curie temperature for a typical ferromagnetic material, the Néel temperature corresponds to the value when magnetic ordering of the charge carriers is no longer hindered by thermal fluctuations and becomes more important than the energy spectrum offered by an interacting Fermi gas.

Given its Fermi liquid characteristics, as well as its potentially high spin-orbit (S-O) interactions, UPt_3 may be a candidate for a new type of material, since the spin and momentum of electrons are locked into patterns governed by chirality, known as a chiral Fermi liquid [16]. S-O interactions come from the coupling of the electron's spin to the angular momentum of its orbit around the nucleus of an atom. This coupling is typically proportional to Z^4, where Z is the nuclear charge of the atom to which the electrons are bounded. In the case of UPt_3, both uranium and platinum atoms have very high Z values, thus it would be reasonable to expect important S-O coupling of its quasiparticles.

In a system where the S-O coupling is strong, it acts as an effective magnetic field, splitting the electron energy levels according to their spins. This is known as the Zeeman effect. Chiral Fermi liquids are therefore 2D interacting Fermi gases where the spin-splitting from S-O coupling dictates the movement of the electrons in chiral patterns, such that electrons only flow in one direction for a given spin (either spin-up or spin-down). The spin sector of such a system can no longer be described by standard Fermi liquid theory, as SU(2) symmetry is broken in such a way that the dynamics of spin can no longer be associated to free quasiparticles. Thermodynamic quantities such as the spin susceptibility are not simply defined by quasiparticles at the Fermi surface, but rather depend on states and momenta between the spin-split surfaces.

2.3 Raman Spectroscopy

At finite temperatures, vibrations in the crystal lattice occur due to thermal agitation of the atoms. One may view these vibrations as being due to harmonic oscillations between atoms, where Coulomb forces act as springs attached to masses, forming a system of coupled oscillators. The allowed vibrational modes of this system of distinct energies can therefore be viewed as quantized energy states, and the waves of vibration through the crystal correspond to quasiparticles known as phonons that carry this energy. Incident light (photons) on the crystal of frequency ω_I will experience inelastic diffusion when the frequency of the diffused light is $\omega_D = \omega_I \pm \omega_p$, where ω_p is the frequency of the phonon in the crystal. When the frequency is additive, the resulting diffusion is known as Stokes diffusion. In the opposite case, the photon loses some energy in order to excite a phonon in the crystal, which is an Anti-Stokes diffusion process. Phonons obtained through this type of diffusion are hence labeled as optical phonons. More generally, optical phonons are independent of the direction of the incident wave vector.

Considering the phonons' energies are dictated by the geometry of the lattice, as well as the masses of the atoms corresponding to the masses from the coupled oscillator picture, extracting the reflected photon energy allows for a spectrum of energy to be measured, from which the nature of the underlying material can be inferred. Figure 2.5 shows such a spectrum for UPt_3, using a polarized laser to measure phonon energies specific to certain crystallographic orientations, at 330 K [17].

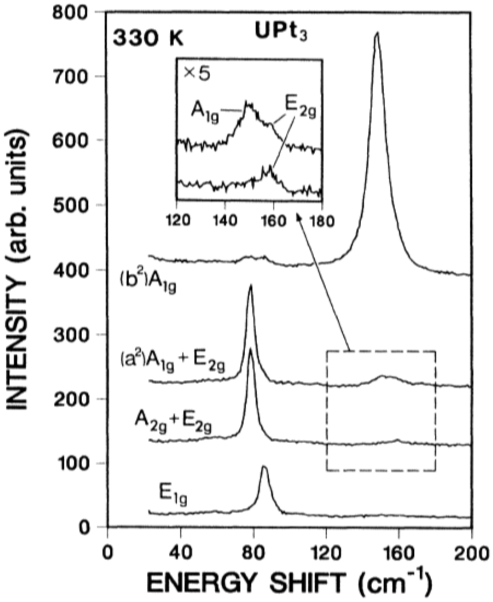

Figure 2.5: Phonon spectrum of UPt_3 at 330 K using the 514.5 nm emission line of an argon laser [17].

2.4 The Superconducting Phase Diagram

Superconductivity according to the ordinary Bardeen-Cooper-Schrieffer (BCS) theory describes the pairing of two electrons (or two holes) which form a Cooper pair once a critical temperature T_C is reached. Where the electron-phonon interaction usually scatters electrons from the atoms of the lattice causing resistance in the material, below T_C this interaction becomes greater than the Coulomb repulsion between electrons, and allows the Cooper pairs to flow uninhibited through the solid. This gives rise to superconductivity; the conductivity becomes infinite, and the supercurrent density is defined by the London equation

$$\vec{j_s} = \frac{-n_s e^2}{m}\vec{A}, \tag{2.8}$$

where n_s is the density of superconducting charge carriers and $\vec{A}$ is the magnetic vector potential. From this equation, one can show all of the interesting phenomena that a superconductor exhibits. However, this model only describes Cooper pairs formed by two charge carriers of opposite spin and momentum. Over the course of the twentieth century, materials were discovered that featured multiple phases of superconductivity, often observed through multiple critical temperatures or critical magnetic field values. Such superconductors which do not obey the standard BCS model are known as unconventional superconductors.

One method of determining phase transitions according to the temperature of the system is through extrinsic properties of the material such as specific heat, defined by the change of internal energy U, according to temperature at constant volume,

$$c = \frac{1}{m}\left(\frac{\partial U}{\partial T}\right)_V . \tag{2.9}$$

Discontinuities in the specific heat as a function of temperature are a direct consequence of these phase transitions. Although $\mathrm{UPt_3}$ was known to be superconducting while also possibly featuring spin-fluctuations [3], its unconventional superconductivity was not specifically shown until a few years later, when specific heat measurements for $\mathrm{UPt_3}$ demonstrated three different phases for a magnetic field perpendicular to the c-axis [18,19]. The H-T phase diagram for $\mathrm{UPt_3}$ is shown in figure 2.6.

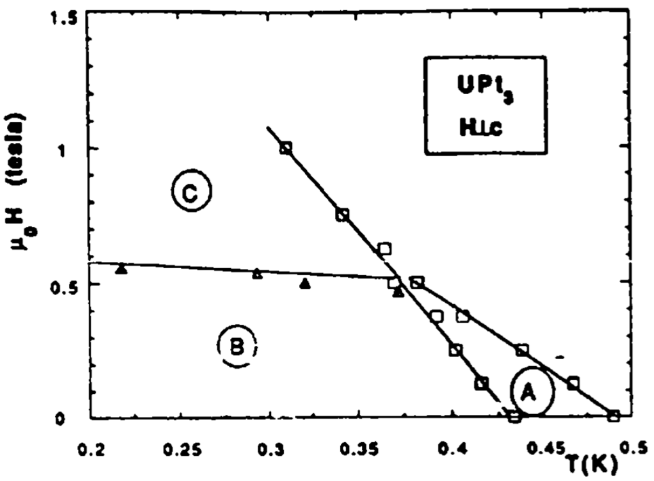

Figure 2.6: Superconducting phase diagram of $\mathrm{UPt_3}$ for the H-T plane, with the magnetic field perpendicular to the c-axis [19]. The three distinct phases, labeled as A, B and C, are illustrated.

The transition from phase A to another phase at H $\approx$ 0.5T is shown through H$_{C2}$(T) data [20,21]. Ultrasonic attenuation measurements according to the magnetic field strength [22] as well as thermal conductivity measurements [23] provide evidence that there is a difference between phases B and C, as shown by the triangular data points in figure 2.6. Sixfold modulation is observed in H$_{C2}$ according to the angle from the c-axis in the basal plane, which disappears as the temperature goes to the tetracritical temperature, noted as T^*, and which reverses sign when $T < T^*$ [24]. Such results provide evidence that there is a difference in the superconducting pairing function between phases A and C. This pairing function is often referred to as the gap function, and will be discussed in more detail in the following section.

It is currently thought that this unconventional superconducting behavior is caused by a coupling between the antiferromagnetism and superconductivity, or rather that the antiferromagnetism plays the role of a symmetry breaking field [4,19,25]. In that way, the spin-fluctuations that allow antiferromagnetic ordering may also be the origin of the attractive interaction between the quasiparticles in the superconducting states. What is not quite understood is how such a small order moment of approximately $0.02\,\mu_B$ can have such a large splitting effect of the critical temperature [24]. The two transitions arise from a splitting of a degenerate state within a single irreducible representation; the symmetry breaking field lifts a twofold degeneracy much in the same way that an external magnetic field lifts the twofold degeneracy of the superfluid A-phase in ^{3}He. In any case, it would seem that this unconventional superconductor is quite different even from other unconventional superconductors, such as high-T$_C$ superconductors, since the multiple phase order parameter of the superconducting state must be characterized by a complex vector with multiple components [26], which will be discussed in the following section.

It has been observed that the difference between the upper and lower critical temperatures at zero field is always of the order of 50 mK, regardless of the sample used [25]. Specific heat measurements according to temperature show a merging of the two transitions for hydrostatic pressures of approximately $p^* = 3.7\,\text{kbar}$, collapsing into a single transition [27]. Figure 2.7 shows this collapse of two phases into one for the T-P plane, which is derived from the data presented in figure 2.8. This can be explained by the fact that moderate pressures annihilate the antiferromagnetic ordering, restoring symmetry to the crystal structure [28].

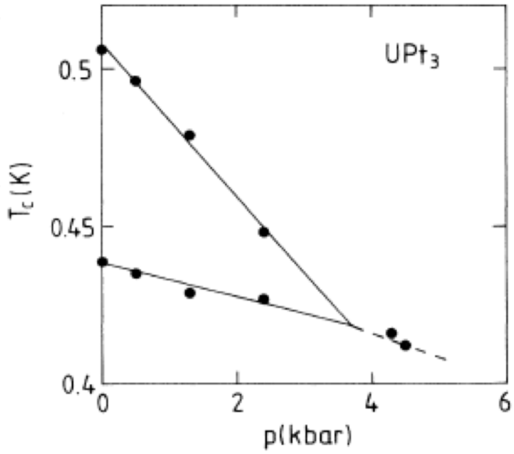

Figure 2.7: Temperature-pressure phase diagram for UPt$_3$ derived from the data in figure 2.8 [27].

2.5 Gap Function

The pairing of two fermions in a superconductor is not solely defined by the type of interaction between the two, but more generally on the way the two parts eventually couple in terms of their spin and momentum. The gap function is typically written as

$$\hat{\Delta}_{\vec{k}} = \begin{pmatrix} \Delta_{\vec{k},\uparrow\uparrow} & \Delta_{\vec{k},\uparrow\downarrow} \\ \Delta_{\vec{k},\uparrow\downarrow} & \Delta_{\vec{k},\downarrow\downarrow} \end{pmatrix}, \tag{2.10}$$

where the arrows signify up or down spin, and $\vec{k}$ is the momentum. In the standard BCS model, where only opposite spin fermions can pair up, the gap function then behaves like an

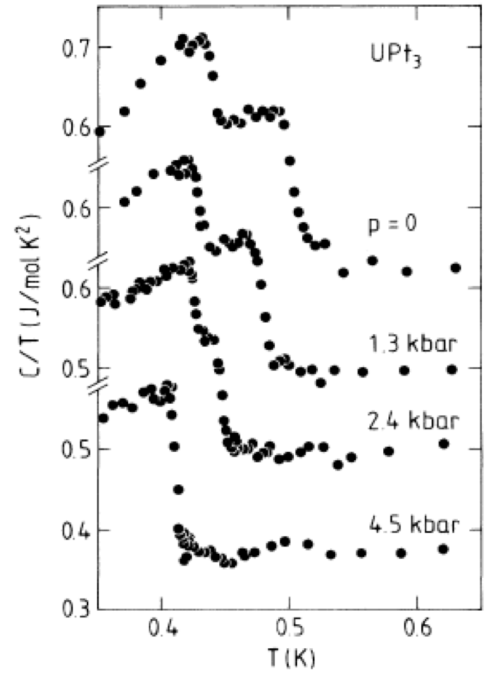

Figure 2.8: Specific heat over temperature as a function of temperature in the vicinity of the superconductive transition for different values of pressure [27].

s-wave, spin-singlet orbital, where

$$\hat{\Delta}_{\vec{k}} = \begin{pmatrix} \Delta_{\vec{k},\uparrow\uparrow} & \Delta_{\vec{k},\uparrow\downarrow} \\ \Delta_{\vec{k},\uparrow\downarrow} & \Delta_{\vec{k},\downarrow\downarrow} \end{pmatrix} = \begin{pmatrix} 0 & \psi(\vec{k}) \\ -\psi(\vec{k}) & 0 \end{pmatrix}, \tag{2.11}$$

with $\psi(\vec{k})$ a scalar function. In the case of spin-triplet pairing, the gap function is written using the conventional vector $\vec{d}(\vec{k})$ such that

$$\hat{\Delta}_{\vec{k}} = \begin{pmatrix} \Delta_{\vec{k},\uparrow\uparrow} & \Delta_{\vec{k},\uparrow\downarrow} \\ \Delta_{\vec{k},\uparrow\downarrow} & \Delta_{\vec{k},\downarrow\downarrow} \end{pmatrix} = \begin{pmatrix} -d_x(\vec{k}) + id_y(\vec{k}) & d_z(\vec{k}) \\ d_z(\vec{k}) & d_x(\vec{k}) + id_y(\vec{k}) \end{pmatrix}. \tag{2.12}$$

The quasiparticle gap is then given by $|\Delta_{\vec{k}}|^2 = \frac{1}{2}Tr\left(\hat{\Delta}^{\dagger}_{\vec{k}}\hat{\Delta}_{\vec{k}}\right)$. From these definitions, one can begin to construct the gap functions for various types of pairings. For example, p-wave pairings (where the total angular momentum is l = 1) are often encountered in the literature, and correspond to $\vec{d}(\vec{k}) = \frac{\Delta_0}{k_F}\hat{z}(k_x \pm ik_y)$ with Δ_0 the amplitude of the superconducting gap and k_F the Fermi momentum. The gap is then $|\Delta_{\vec{k}}|^2 = |\Delta_0|^2 \frac{k_x^2+k_y^2}{k_F^2}$, where there are nodes along the gap for $k_x = k_y = 0$ when $k_z = \pm 1$ Incidentally it is due to such nodes in the gap function, or lack thereof, that one may characterize the gap function of a superconductor.

Like any other wavefunction encountered in quantum mechanics, the overall energy of the system, i.e. the Hamiltonian, can be quite complex and therefore determining its features through symmetry considerations allows for an efficient way of developing a model for a given system that obeys a given set of transformations that leave it unchanged. For example, U(1) gauge symmetry denotes a system's invariance to a phase, corresponding to the transformation

$$\hat{\Phi}\psi(\vec{k}) = e^{i\phi}\psi(\vec{k})$$

with ϕ being the phase acquired by the wavefunction. One such transformation corresponds to the orbital rotation symmetry of the system, which is limited by the point group of the lattice of the material. It is therefore common to construct the order parameter of the superconducting pairing based on the irreducible representations underlying the point group of the lattice. As discussed in a previous section, UPt_3 belongs to the D_{6h} point group, thus its superconducting pairing in each of its phases must be represented by one of the irreducible representations of said symmetry group. When going from one phase to another, one or more symmetries are broken, resulting in a reduction of the possible irreducible representations to construct the symmetry group associated with the new phase. If going from phase 1 to phase 2 breaks time-reversal symmetry (TRS), then the new symmetry group must contain the irreducible representation which is contained in both groups that is invariant under TRS. In that way, if a superconducting phase is invariant under TRS, then its order parameter must be defined by an irreducible representation which is also invariant under TRS. Knowing this, one may consider the experimental and theoretical evidence which may shed some light on the exact nature of the unconventional superconductivity in UPt_3.

For instance, thermal conductivity measurements have helped show the presence of nodes along the c-axis in the B-phase, in addition to the line node in the basal plane as determined through previous experimental results [4,29]. These nodes seemed to be of line and quadratic point structure, leaving the E_{2u} representation for this phase. It was then shown theoretically, by analyzing the Fermi surface and gap function more precisely, that both the E_{2u} and E_{1g} representations are viable solutions for the gap function according to the thermal conductivity data [10,30].

Other experiments have shown instead that the E_{1g} and E_{2g} could not work, though with the support of group theoretical studies the E_{1u} representation with f-wave character could fit the results of the data [31,32]. Later work using spin susceptibility showed an inconsistency with these results [5].

This back and forth in the determination of the order parameter has continued as such to this day. By now, it is mostly agreed upon that the B-phase breaks TRS [33,34]. Since a general multi-component superconducting order parameter can break time-reversal symmetry only if it belongs to a representation of dimension greater than one, the order parameter must therefore belong to one of the four different 2D representations of D_{6h}, which is supported by the experimental data thus far. This breaking of TRS is what often garners UPt_3 with the title of a *chiral superconductor*, as the TRS-breaking is a feature most notably associated to the effect of a magnetic field on a material, which is consequently quite similar to that which was discussed for the chiral Fermi liquid concept.

Despite all of the contradicting evidence, most experimental evidence and theory deems the E_{2u} representation worthy of the heavy burden that is explaining the multiple superconducting phases [35,36].

	A Phase	*B* Phase
E_{1g}	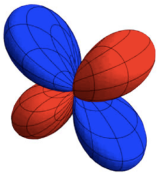 $\Delta(k) = \Delta(T)k_x k_z$	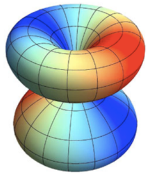 $\Delta(k) = \Delta(T)(k_x + ik_y)k_z$
E_{2u}	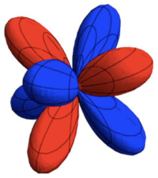 $\bar{d}(k) = \Delta(T)(k_x^2 - k_y^2)k_z\hat{z}$	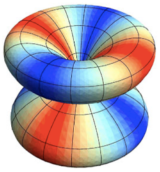 $\bar{d}(k) = \Delta(T)(k_x + ik_y)^2 k_z\hat{z}$

Figure 2.9: Order parameter of the A and B phases, for both E_{1g} and E_{2u} [36].

Chapter 3

Experimental Methods

3.1 Device Preparation

This section is separated into two distinct parts which are necessary for developing a device to be used in various measurements. The first part focuses on obtaining suitable flakes of the material through a fracturing method, followed by the fabrication of a device made from those flakes with usable contacts to later probe it directly.

3.1.1 Micromechanical Fracturing

Materials whose layers are bound together by van der Waals interactions have gained much interest in the field of two-dimensional materials due to the fact that they may be exfoliated easily through mechanical methods, separating the material atomic layer by atomic layer. This widespread interest initially took off following the discovery of graphene by Novoselov and Geim at the turn of the century, where the use of adhesive tape could produce atomically thin layers of graphene from bulk graphite fairly rapidly. Unlike these van der Waals bonded materials, UPt_3 is, as discussed in the previous chapter, a crystalline metal. Although the strength of the interactions between layers along the c-axis is not known, it is greater than that of van der Waals bonding, preventing us from relying on such simple mechanical exfoliation means to which we are used to adhering.

A new method of mechanical exfoliation was thus necessary to obtain thin flakes of UPt_3, where the force used to divide the layers of the materials is sufficient to essentially break the material apart. Micromechanical fracturing was performed with a pestle and mortar, made from a white ceramic. Small pieces of bulk UPt_3 were cleaved from the original crystal, and were then placed into the mortar. Using the pestle, one could successfully crush the small fragment of material into a powder, consisting of flakes of various shapes and sizes, hence the use of the term *fracturing* rather than *exfoliating*. Once the powder was sufficiently ground, a piece of adhesive tape is used to collect the ensuing flakes, which can then be transferred to a silicon substrate for further use. Figure 3.1 illustrates the process used. Alternatively, small pieces of polydimethylsiloxane (PDMS) with low adherence can be used to facilitate the amount of flakes transferred onto a substrate.

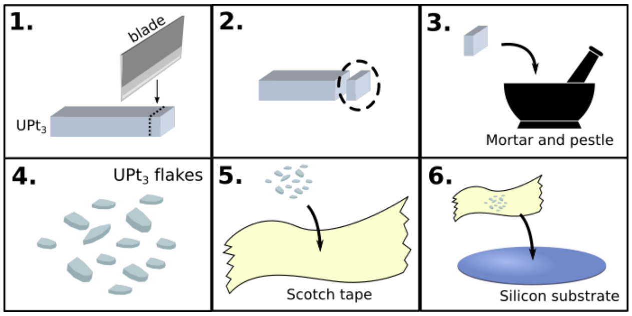

Figure 3.1: Micromechanical fracturing process of UPt_3 flakes. A small piece of the UPt_3 crystal is cleaved using a sharp razor blade, and is then placed in a mortar to be ground down into small flakes. These are then transferred to a substrate with adhesive tape.

Once the transfer is complete, an initial characterization of the flakes then follows, which is key before going through to the process of designing a pattern for electron beam lithography (EBL).

The pitfall of this technique is that flakes obtained through such a rough method are not smooth, so they adhere very little to the substrate's surface. An SEM image of a piece of UPt_3 obtained via this technique is shown in figure 3.2 where the jagged and uneven surfaces are apparent. Further problems arise when attempting to find flakes that are thinner than one micron, as this technique does not directly cleave layers apart along their basal planes; rather the crushing procedure reduces the size of flakes volumically, therefore the thickness of flakes is generally comparable to the surface size. A further analysis of the flakes obtained is described in the following section.

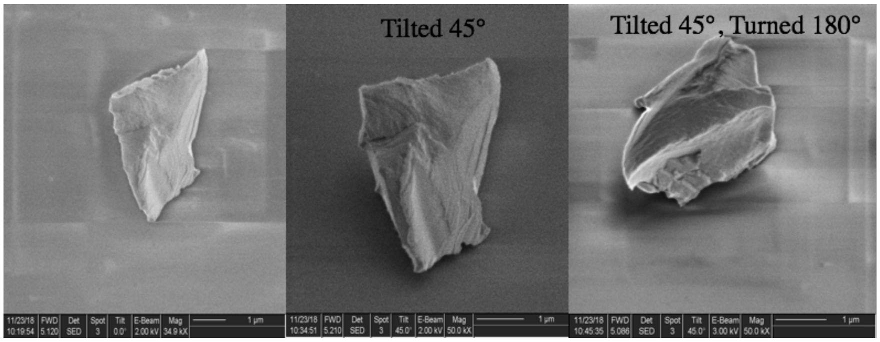

Figure 3.2: SEM images of UPt_3 flake S14-75. The first image shows the small piece from above, the second shows the flake for a tilted stage at an angle of 45° whereas the third is at 45° turned 180° around.

Given the terraced structure of the bulk UPt_3 crystals, as shown in figure 3.3, it would be ideal to precisely peel away a thin piece of the material, providing flakes in a more controlled way that would likely induce far less disorder in the crystal structure. Such a technique was attempted by utilizing a diamond-tipped scribe mounted on a micromanipulation stage. The stage itself allows for sub-micrometer precision movement in three dimensions, while the diamond tip of the scribe is hard enough to break apart the surface of the UPt_3 crystal while being small enough so as to limit the size of the flakes that are removed from the bulk crystal. The bulk crystal is held in place underneath the objective of an optical microscope while the scribe is moved slowly toward the sample, allowing for a very precise extraction of flakes that can be viewed in real-time. Figure 3.4 features a demonstration of this flake extraction.

Drawbacks of this fracturing technique are two-fold. For one, the tip of the scribe is still

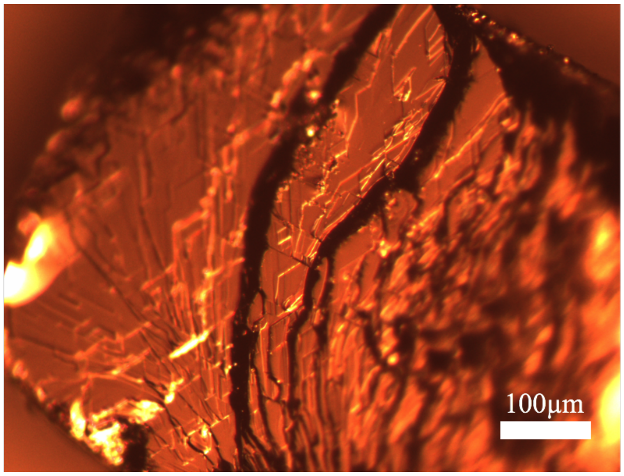

Figure 3.3: Optical microscopy image of a bulk piece of UPt_3 obtained by cleaving the initial crystal with a razor blade, along the basal plane. The presence of the terraces show that this cleaving is not perfectly down the basal plane, however.

rather large, thus the pieces it can remove will be large as well, and since UPt_3 tends to break apart in chunks rather than flake apart the pieces will also remain rather thick. This could possibly be remedied by using a tip with an even pointier end. Nevertheless, flakes that are successfully peeled off from the bulk sample and adhere to the end of the scribe's tip are difficult to securely place onto a substrate for later use without scratching the surface of said substrate, thus losing the flake among debris. Substrates made of SiO_2/Si as well as some made of PDMS have been used to deposit the flakes on, however the same issue occurs for both, the latter being easily damaged by the scribe tip due to its low rigidity.

A device can then be made with flakes whose size and shape are deemed optimal based on microscopic imaging. In order to fabricate devices with flakes that range in surface size from hundreds of nanometers to tens of micrometers, EBL is necessary.

3.1.2 EBL Procedure

Electron beam lithography is performed by exposing parts of an electron-sensitive resist layer, which is spin coated on the substrate, where the exposure pattern and time are decided using

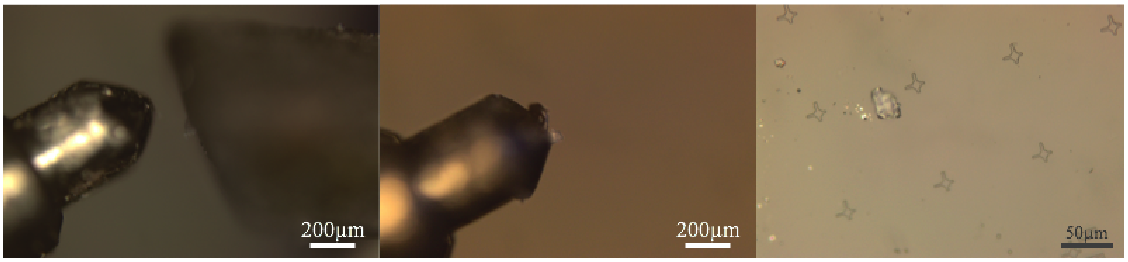

Figure 3.4: Mechanical fracturing technique using the diamond-tipped scribe. The left image shows the scribe approaching the bulk UPt_3 sample in order to scrape off a flake, while the middle image features a large piece of UPt_3 stuck on the end of the scribe which is then deposited directly onto a PDMS substrate as shown in the image on the right. The irregularly-shaped feature on the substrate is not the flake itself, but rather a crater where a chunk of PDMS was torn off, while the scribe gently rubbed the surface in order to deposit the flake.

a specialized software.

Two different layers are typically used for EBL; a first layer of 9% methyl methacrylate in ethyl lactate (MMA EL9) and a second layer of polymethyl methacrylate (PMMA). The former is more sensitive for a given electron exposure, allowing for an undercut in the bottom layer of the resist that will ease the lift-off procedure later on. An example of this is illustrated in figure 3.5. The two layers are each spun at 3000 RPM for 30 seconds, then baked at 175°C for fifteen minutes, allowing for a total thickness of 500 nm of resist on top of the substrate.

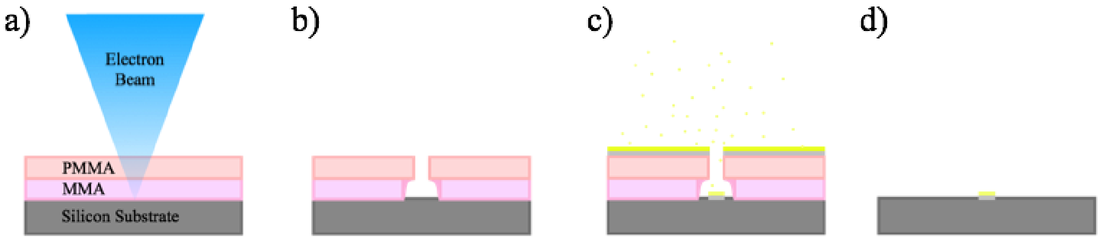

Figure 3.5: **a)** Illustration of the PMMA and MMA resist layers on a substrate being exposed to an electron beam during EBL, and **b)** the same layers after the development process followed by **c)** the metal deposition and **d)** lift-off procedures.

Before making an actual pattern on a flake of interest, a dose test is necessary in order to avoid over- or under-exposing the EBL resist layers. This is typically done by designing a repeating pattern of varying doses on a single write-field. Once the development process is complete, the pattern will become visible and then it is possible to determine which dose factors yielded the best results. An example of such a pattern design using the EBL software, along with the resulting pattern in the resist layers is shown in figure 3.6.

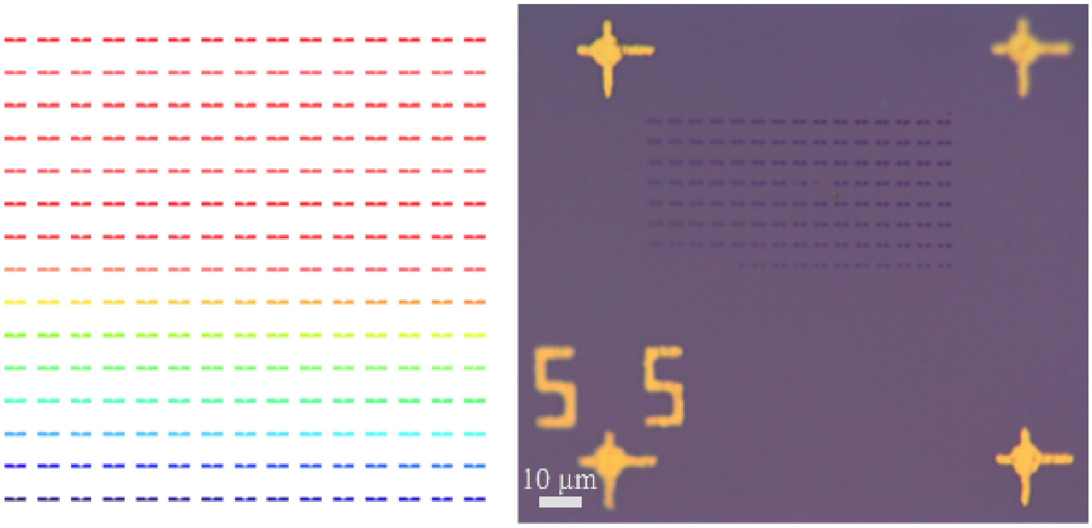

Figure 3.6: Pattern designed using eLine Plus for a dose test (left) and the resulting pattern (right). The dose factor begins at 0.00 on the bottom left corner of the pattern, increasing by intervals of 0.01 to the right and by 0.2 upwards.

Doses ranging from $150\,\mu\mathrm{C\,cm^{-2}}$ for features larger than $10\,\mu\mathrm{m}$, to $250\,\mu\mathrm{C\,cm^{-2}}$ for features on the order of $1\,\mu\mathrm{m}$, or less.

Patterns for EBL are made using the eLine Plus software, which is also used to control the stage and electron beam of the Raith electron microscope at Polytechnique Montréal. Figure 3.7 is an example of a pattern that was used for EBL, created with eLine Plus. The electron microscope is set up to run at 20 kV, though it could go up to 30 kV, and is set to a working distance of 10 mm. These parameters have been optimized by the technicians to deliver high resolution and reliability in patterning features of various scales. Once a flake has been selected to be used for a device, a picture of the flake at 50x zoom using an optical microscope is taken to be used as a reference. The gold crosses on the substrate are useful for properly aligning the image for designing a pattern, as well as a coordinate system for the alignment of the EBL process. Ideally, the flake to be patterned should be situated within four gold crosses, and the center of the working area of the pattern should be centered in the middle of the four crosses. Therefore the pattern in the software uses the exact same coordinate system as the real coordinate system of the substrate. As is shown in figure 3.7, the flake is drawn using the coordinates of each of its corners, obtained by counting the pixels of the image taken through optical microscopy. Once the exact size and location of the flake is determined in the software, the pattern is designed around it, ideally making two different layers to account for large and small features. Large features, such as the large pads, are used in most designs and therefore need not be redesigned each time. Having a dedicated layer for the small features alleviates the need to remake an entire pattern from scratch each time, requiring only the contacts which connect to the flake to be remade for each new flake. With a meticulously designed and aligned pattern, the exposure process can be performed by uploading the desired pattern to the software and running it.

After the resist is exposed to the electron beam, the development process takes place in three steps. First, the sample is put into a 1:3 solution of methyl isobutyl ketone (MIBK) and isopropyl alcohol (IPA) for thirty seconds, followed by an IPA bath for one minute, then a bath in de-ionized water to fully halt the development process. During each of the steps, it is important to agitate the sample in order to completely cover the surface and wash the activated portions of the resist away. Once this is complete, the sample is removed from the water and is promptly dried with a nitrogen gun, preventing residue or dust from contaminating the surface. The sections of the resist which were exposed to the electron beam are dissolved in the MIBK/IPA solution, leaving a trench-like structure to be used as a stencil for the metal deposition to come. Since the MMA is more sensitive to the electron exposure, a larger portion is activated and hence dissolved in the development, leaving the

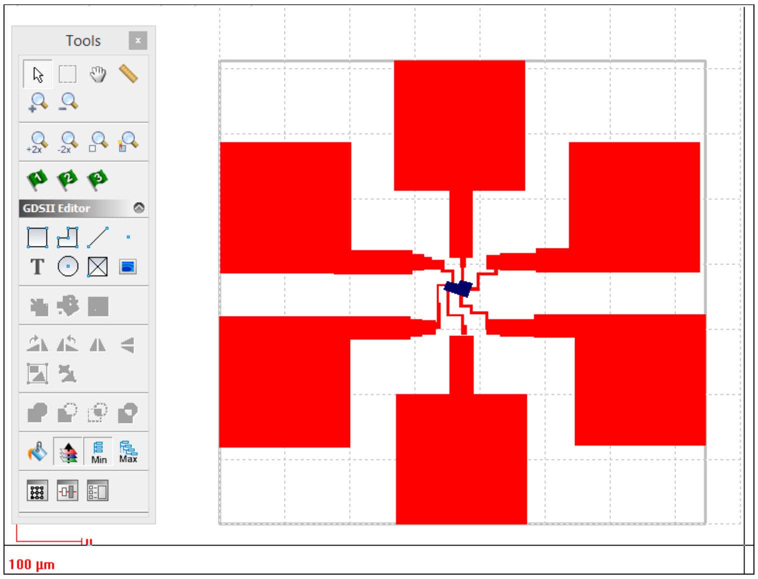

Figure 3.7: Example of a pattern for a Hall bar geometry on flake S3-86, designed using eLine Plus. The red areas designate features to be patterned, whereas the blue area represents the flake, which will not be exposed to the electron beam.

undercut as previously mentioned. This is illustrated in figure 3.5. As such, the sample is ready for metal deposition.

Metal deposition is performed using an electron beam evaporation system. 10 nm of nickel or titanium are deposited before the desired metal, such as gold, in order for the gold to adhere better to the substrate's surface. Typically 80 nm to 100 nm of gold are then deposited to make the contacts; if the contacts are any thinner, they may suffer significant damage from the probe station tips or the wire bonding procedure later on. Therefore, it is important to have at least 100 nm of metal for the contacts.

The rest of the resist is then removed by submerging the sample in acetone, heated on a hot plate to roughly 60 °C. It is recommended to gently stir the acetone around using a pipette, as the deposited metal will adhere quite well to any edge of the substrate that does not have much resist on it. If the current of the acetone around the substrate is too violent or turbulent however, the smaller contacts which are quite fragile may be accidentally ripped off. Alternatively, peeling off a corner of the deposited metal with fine tweezers to expose some of the resist, acting as a channel for the acetone to get underneath the rest of the metal, may also be an efficient lift-off technique while erring on the side of caution.

Following these steps, the excess metal will be removed along with the rest of the resist layers, leaving only the portions where the resist was developed, as illustrated in figure 3.5. As long as the metal deposited is less than roughly 250 nm, the undercut obtained in the MMA layer should allow for sufficient space around the deposited metal contacts and the resist, preventing any of the metal from being damaged during lift-off. The substrate should then be removed from the acetone and dried off gently with nitrogen. Figure 3.8 shows the resulting Hall bar geometry obtained from the same flake used for the pattern design in figure 3.7 after the metal deposition procedure.

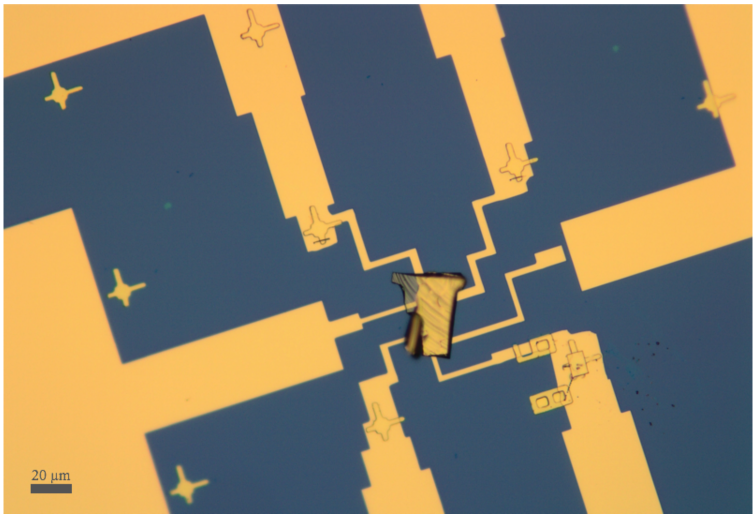

Figure 3.8: Optical microscope image of flake S3-86 with 100 nm of Au/Ti deposited via electron beam evaporation.

3.2 Characterization and Analysis

3.2.1 Microscopy

Throughout the many steps preceding the obtention of a full-fledged device, it is key to properly characterize the size of the flakes to be used, as well as their thickness and overall geometry using a combination of optical microscopy (OM), atomic-force microscopy (AFM) and scanning electron microscopy (SEM).

Initially, once a large piece of the bulk UPt_3 is fractured and the flakes are transferred to a substrate, OM is a quick and efficient way to scan the surface of the substrate for flakes that were successfully transferred from the adhesive tape. An image of the substrate covered in such microscopic flakes is shown in figure 3.9. Given the metallic nature of UPt_3, a closer inspection using OM at greater magnification is necessary to determine whether the surface of a given flake is highly reflective, since this may not always be clear at low magnification. Varying the intensity of the lamp on the microscope also allows to observe the difference in the reflectivity of the flakes as opposed to the substrate, facilitating in the determination of metallic flakes compared to non-metallic ones. Similarly, one could compare the reflectivity of flakes to that of the gold (metallic) crosses of the substrate. Finally, the dark field setting on the microscope emphasizes areas where the elevation changes, such as at the edge of a flake or the terraces on their surface. Figure 3.10 shows the same section of the substrate as figure 3.9 with the dark field setting on, where some of the much smaller flakes become more visible at low magnification.

Designing a pattern to be used for EBL requires an image of the flake with sufficient resolution so as to distinguish each of its sides, as well as to determine its exact position in relation to the four gold crosses around it. As such, an image with 50× magnification is optimal, as it allows for high resolution without cutting out the surrounding crosses.

Figure 3.9: Optical microscope image at 10x magnification of position 36 on substrate #2 with UPt_3 on its surface.

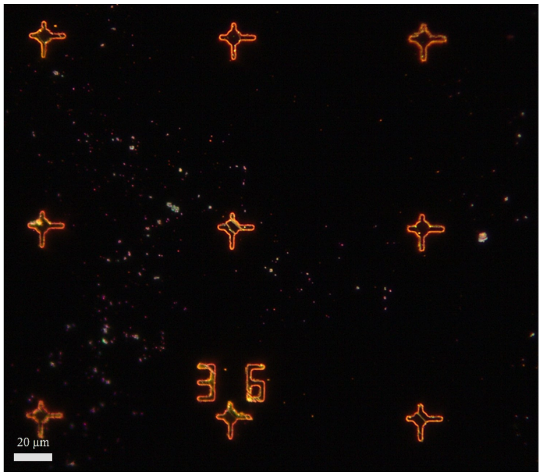

Figure 3.10: Optical microscope image at 10x magnification with the dark field setting of position 36 on substrate #2 with UPt_3 on its surface.

Centering and aligning the image using the gold crosses eliminates a certain amount of error that may prevent the final pattern from being precisely aligned with the flake itself.

One of the main interests of this project is to determine the nature of UPt_3 when its thickness approaches the order of the coherence length of the superconducting state, of the order of 10 nm. Determining the thickness of the flakes produced in the fracturing process is paramount, and AFM provides a direct avenue to that goal. Small flakes close to 40 nm have been observed, as shown in figure 3.11. A histogram of the flakes observed through AFM is presented in figure 3.14, demonstrating the variety of flake thicknesses below 1 µm obtained over time.

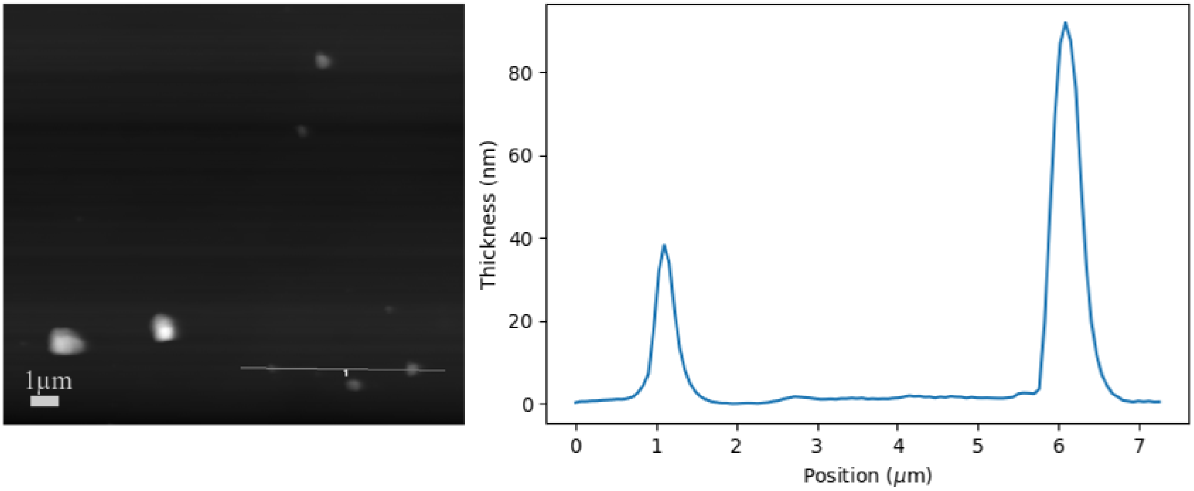

Figure 3.11: AFM image of the UPt_3 flakes on substrate #2 near position 36, along with the thickness profile corresponding to the line indicated on the picture.

A couple of disadvantages with AFM are the amount of time it requires to scan a given area with high enough resolution to distinguish features below a micron, as well as the fact that only the top part of the sample is scanned. One cannot scan the general shape of the flake in question, only the surface. This is when scanning electron microscopy (SEM) becomes necessary. The SEM sample stage can be rotated 180° around to allow viewing the sample from all sides, but most importantly the stage can be tilted to 45° so as to scan the sides of the sample. Furthermore, SEM is a much quicker process; scouring the substrate's surface for important features and scanning the features themselves is done with the same apparatus, whereas AFM requires searching for the small features of interest using a camera, then scanning the selected area with the AFM tip to ensure that the object of interest is indeed there. SEM scans themselves are often much quicker, of the order of a few seconds. One can perform longer scans over minutes in order to get higher quality images, although

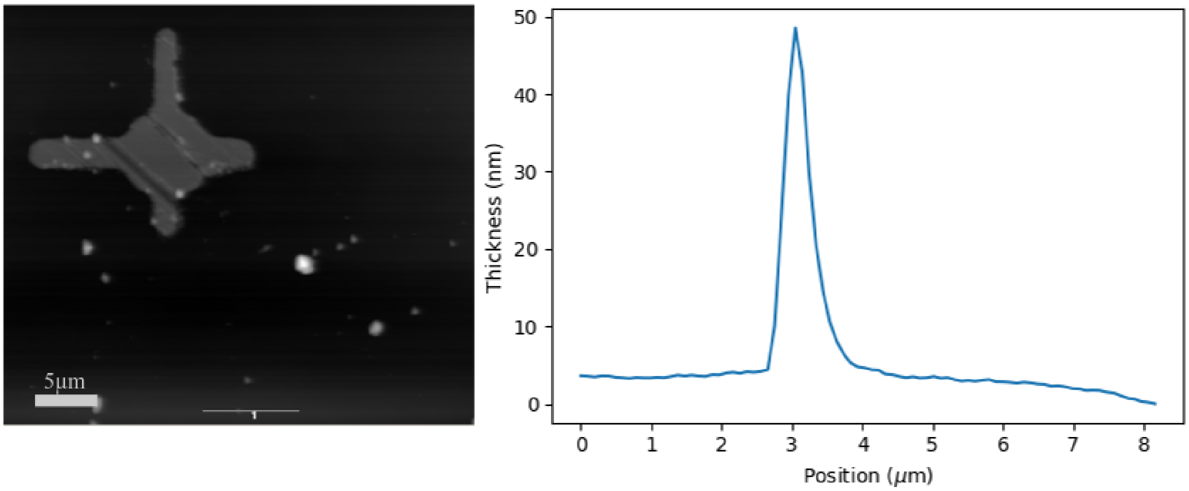

Figure 3.12: AFM image of the UPt$_3$ flakes on substrate #2 near position 36, along with the thickness profile corresponding to the line indicated on the picture.

the short scans without averaging often present the user with sufficient data for a quick analysis.

SEM was notably used in order to study the geometry of the flakes obtained through the micromechanical fracturing technique. Figure 3.2 shows a piece of UPt$_3$ acquired through this method, which does not have a typical flake-like structure, instead being uneven and irregular. Such a shape hinders the fractured UPt$_3$'s ability to adhere to the substrate through van der Waals forces, providing an explanation as to why it is so difficult to keep them on the surface while spin coating or performing the lift-off procedure. The devices that were made did not show any conduction at room temperature, regardless of the gate voltage applied or the amplitude of the voltage applied from source to drain, which will be explained further in the following section. Verification of the quality of the contacts on the samples was not possible using only OM, therefore SEM allowed for much more detailed images to troubleshoot the issues. Figure 3.15 shows a time-line of the fabrication of a device, most notably an SEM image of the device at 45° which proves why there was no conduction through the device. Simply relying on an OM image or an AFM scan would not allow the

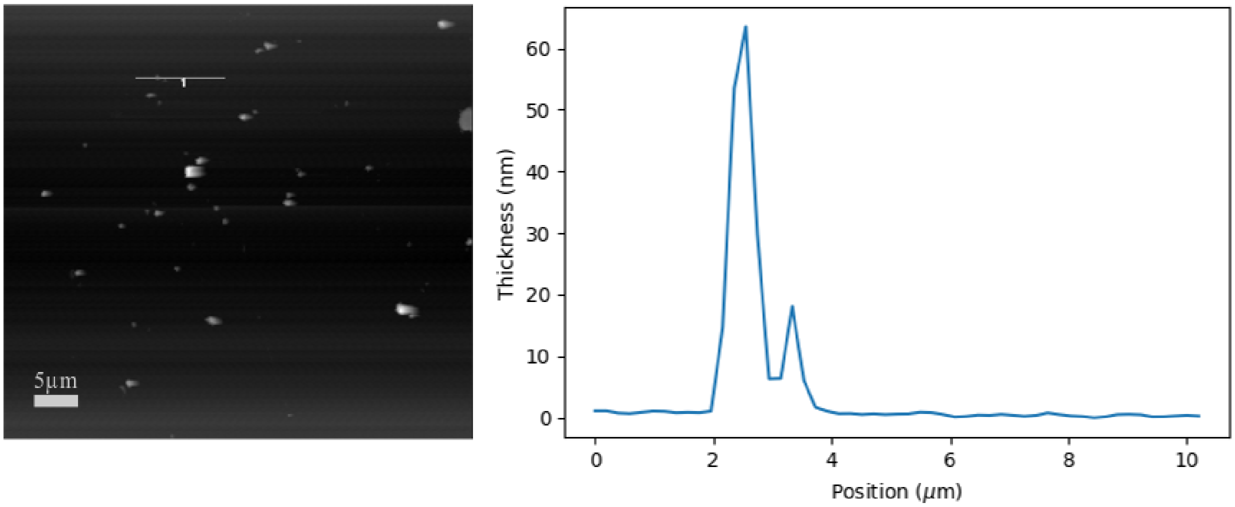

Figure 3.13: AFM image of the UPt_3 flakes on substrate #2 near position 68, along with the thickness profile corresponding to the line indicated on the picture.

resolution, nor the necessary angle to observe that the contact does not cover the side of the flake, leading to an open circuit. Figure 3.16 shows a time-line for the fabrication of a device at position 37 on substrate #9 (S9-37). Here the SEM image provides sufficient resolution so as to determine that the spot seen under OM where the flake was located turns out to only be the spot of the gold contacts that is broken off, as the flake was likely dislodged during the lift-off process.

3.2.2 Electronic Transport Measurements

Before putting a device in a fridge with high magnetic fields in order to study electronic phenomena at ultra-low temperatures, it is quite insightful to simply study the two-point resistance of the sample at room temperature. The simplest and quickest method is by using a probe station. The setup used in our laboratory comprises an Agilent B1500A semiconductor device analyzer connected by coaxial cables to a set of indium needles, which are used to connect to the large ohmic contacts of the device, located inside the high-vacuum enclosing of a Janis ST500 probe station. The needles can be controlled by means of

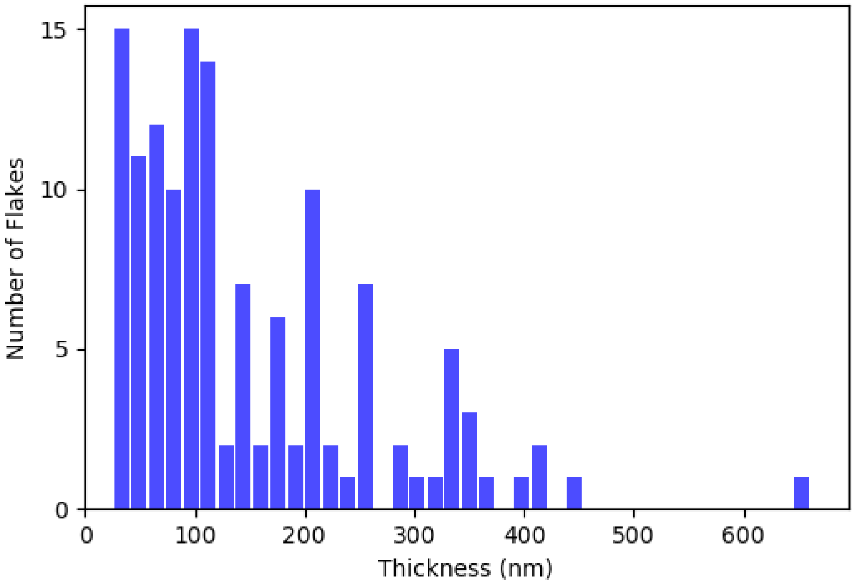

Figure 3.14: Histogram of flake heights obtained through micromechanical fracturing of UPt_3, measured using AFM.

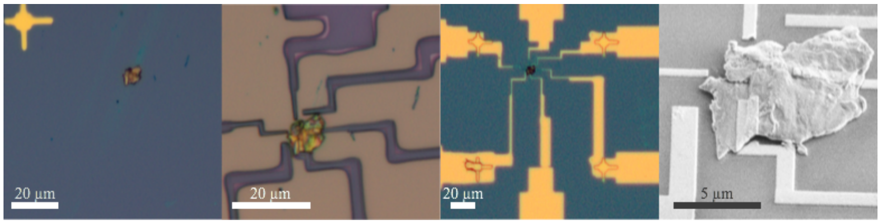

Figure 3.15: Time-line of the fabrication of a device for flake S4-44. The first image is an OM image for preparing the EBL pattern, the second image shows the flake after developing the substrate following the EBL exposure, while the third image shows the gold contacts on the flake following the metal deposition steps, with the final image showing an SEM scan of the device at a 45° tilt angle.

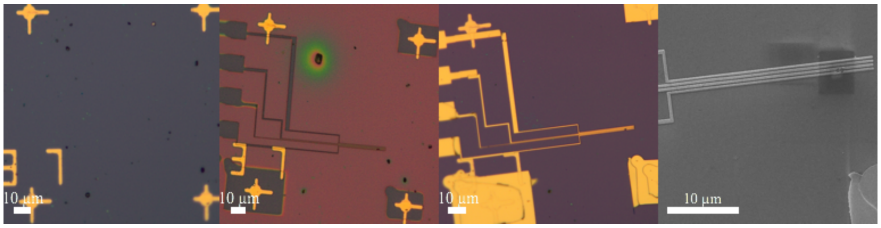

Figure 3.16: Time-line of the fabrication of a device for flake S9-37. The first image is an OM image for preparing the EBL pattern, the second image shows the flake after developing the substrate following the EBL exposure, while the third image shows the gold contacts on the flake following the metal deposition steps, with the final image showing an SEM scan of the device.

a micromanipulation stage, allowing a gentle and precise contact with the large metal pads made using EBL. Each needle can be used as a source or drain, and a voltage up to 30 V can be applied to the base on which the device rests inside the probe station, so as to apply a back gate potential. The top of the probe station casing features a small glass window, through which an optical microscope connected to an external monitor allows to view the needles in real-time, facilitating the manipulation on a microscopic scale.

Once the needle probes are in place on the desired contacts of the device, the system can be programmed to sweep across a predetermined range of voltage, with a given step size. Simultaneously, the program can measure the two-point current at the pins, while a current threshold is in place for the safety of the sample, and displays the graph evolving in real-time on the Agilent parameter analyzer itself. As such, quick I-V curves for different back gate values and for a variety of contact configurations can be obtained, probing the resistance of the material along different directions.

A small fragment was removed from the bulk crystal of UPt_3 and placed onto a silicon substrate and put inside the probe station, where an initial I-V curve was obtained as a benchmark. This is shown in figure 3.17, where the red and blue curves represent the source and drain currents respectively, while the green curve corresponds to the gate signal whose scale goes up to 100 fA and down to 1 fA on this graph. Apart from some minor hysteresis, no noteworthy features are present in these curves, though we may infer an approximate resistance of $10\,\Omega$ from Ohm's law, which corresponds to a metallic substance.

Following this, devices prepared with various flake sizes and thicknesses were to be studied using the probe station. However, every sample prepared showed no signal for any range of voltage or gate voltage applied. Figure 3.18 shows an example of an I-V curve measured for a device made from UPt_3 flake S9-37, with a gate voltage of 10 V. The currents obtained simply fluctuate around the noise level of the order of 10 fA, corresponding to an open circuit.

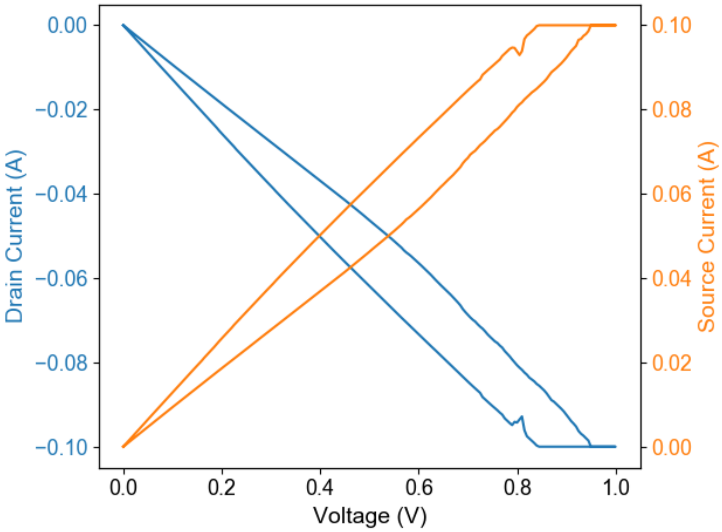

Figure 3.17: I-V curve for a bulk sample of UPt_3, where the orange and blue curves represent source and drain data respectively, while a gate voltage of 1V was applied.

Evidence in the form of SEM imaging confirmed the suspicious open circuits for all of the devices prepared for this purpose, whereas this type of signal might have indicated a highly resistive layer between the contacts and the flake's surface. That said, sufficiently elevated voltages would be expected to burn through thin insulating layers. One could potentially use a focused ion beam (FIB) in order to repair the open circuits by depositing platinum where the contacts do not reach the flake.

3.2.3 Raman Spectroscopy

Polarized Raman spectroscopy was performed on some small flakes of UPt_3 that were obtained using the micromechanical technique, in order to ensure that these flakes were indeed UPt_3. A 532 nm laser was used, along with three Bragg filters in order to observe the Raman peaks at lower frequency values. Figure 3.19 shows the Raman spectrum for a bulk piece of UPt_3, obtained by cleaving the crystal with a razor blade, as well as the background of the SiO_2/Si substrate on which the piece of UPt_3 was placed. These signals were obtained by

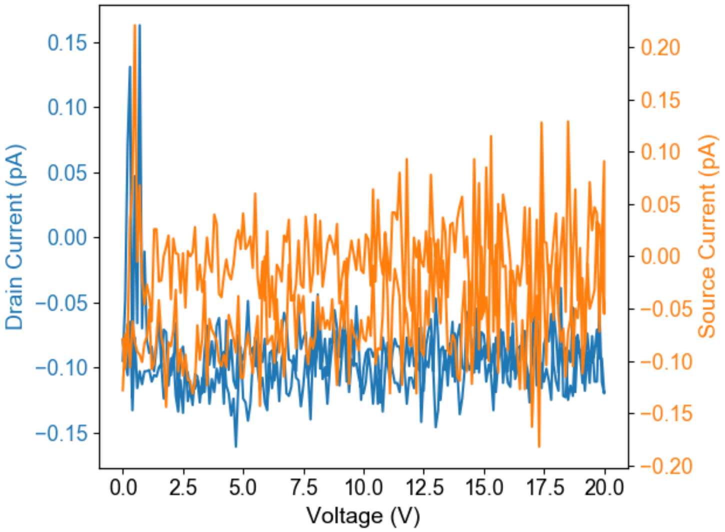

Figure 3.18: I-V curve for UPt_3 flake S9-37, where the orange and blue curves represent source and drain data respectively, while a gate voltage of 10V was applied.

averaging over multiple scans, in order to resolve the smaller features. The peak at roughly $80\,\text{cm}^{-1}$ corresponds to the E_{1g} phonon [17]. The other features seen in the SiO_2/Si data, such as the broad peaks from $200\,\text{cm}^{-1}$ to $450\,\text{cm}^{-1}$ and the large peak at $520\,\text{cm}^{-1}$, correspond to that of the substrate [37,38], or simply features due to the laser itself. The other narrow, sharp peaks around 30, 60, 66, 200, 300, 420 and $590\,\text{cm}^{-1}$ are simply artifacts of the measurement.

The intensity of the $80\,\text{cm}^{-1}$ is quite low, which indicates that even cleaving the crystal with a razor blade may induce a significant amount of disorder of the crystalline structure. This disorder is worsened when the micromechanical fracturing technique is performed, as was made evident when attempting to scan the flakes on substrate #2. No peaks corresponding to UPt_3 were observed for the flakes near position 36 on the substrate (see figure 3.9); only spectra resembling the background signal of the substrate were measured, even for flakes roughly 20 µm across, much larger than the spot size of the laser. It would therefore be of the utmost importance to develop an exfoliation technique which does little to hinder the crystal structure, if one wishes to characterize the flakes via Raman spectroscopy. Otherwise, techniques such as X-ray photoelectron spectroscopy (XPS) may be of use as a non-destructive means of characterizing the nature of the flakes.

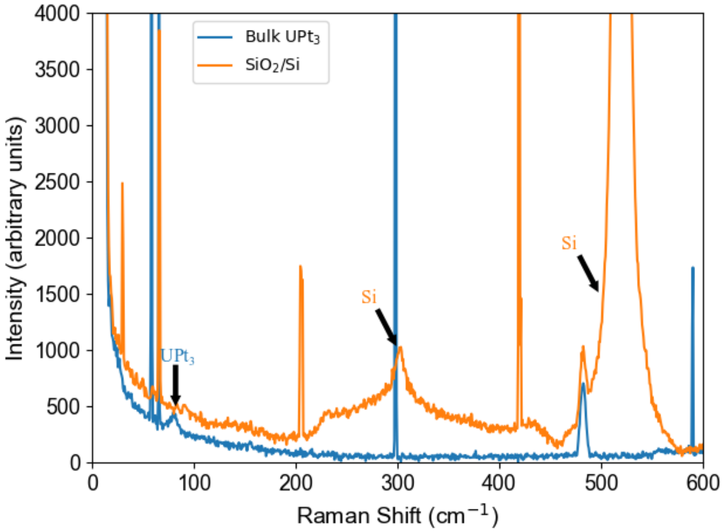

Figure 3.19: Raman spectroscopy data for a bulk piece of UPt_3 placed on a SiO_2/Si substrate. The data in blue corresponds to the spectrum obtained by averaging 5 scans on the UPt_3 sample, whereas the orange data is the background (substrate) spectrum.

Chapter 4

Conclusion

UPt_3 hosts a variety of interesting phenomena that have yet to be fully explained with our current understanding of heavy Fermi liquid theory and superconductivity, thereby ensuring a plethora of possible outcomes when the charge carriers inherent to both of these concepts are confined to two dimensions. Micromechanical fracturing of bulk crystal samples has been performed, producing flakes below 1 µm in thickness, down to approximately 40 nm, which were analyzed using AFM and SEM. EBL was then used to attempt to contact these flakes, in order to measure electrical and thermal conductivity in these samples, however the irregular surface of the flakes obtained through this rather coarse fracturing method prevented any flakes from adhering to the substrate during the spin-coating or lift-off processes. Furthermore, these flakes showed none of the expected phonon peaks during Raman spectroscopy, whereas large pieces of the bulk sample displayed a faint signal at the $80\,\mathrm{cm}^{-1}$ frequency shift value which shows how this fracturing method introduces excessive disorder in the lattice structure of the flakes. A bulk sample was analyzed using the probe station, where a two-point resistance of $10\,\Omega$ was measured, corresponding to a resistivity of approximately $0.5\,\Omega$ cm, which is much higher than that reported in the literature of approximately $230\,\mu\Omega$ cm in high quality samples [14]. The large discrepancy may be due to poor contact with the UPt_3 surface from an oxide, or the wiring resistance in this two-point resistance measurement setup is too large to observe the low resistance of our samples.

Based on these results, it would be of utmost importance to develop a technique of mechanical exfoliation that is far more precise, allowing for cleaving parallel to the basal plane of the crystal which would yield far cleaner surface topographies and inducing less disorder in the crystal as well. One may also consider foregoing mechanical exfoliation, instead opting for a chemical etching technique to thin down large area bulk samples. Once atomically thin flakes are obtained, any experiments done to study the order parameter of the superconducting phases should be performed, since the reduction from an effectively infinite layered structure to one with finite layers would inherently break translational invariance along the c-axis, owing to the breaking of the vertical inversion symmetry included in the D_{6h} point group. This in turn would reduce UPt_3 to the D_6 point group, therefore inspecting the nodes in the gap function would allow one to determine the irreducible representation belonging to both the bulk and 2D regimes, which could put an end to the discussion on its superconducting nature. However, it is likely that superconductivity might be eliminated completely below a certain thickness; once the superconductor thickness is smaller than the coherence length of the Cooper pairs, superconductivity should no longer be permitted. Some cases of superconductivity being observed in atomically thin films have been reported, such as in $NbSe_2$ [39], although the exact nature of this kind of 2D superconductivity is still debated.

In the case where superconductivity is suppressed in a 2D regime, one could investigate the potential chiral nature of the Fermi liquid in the normal state through angle-resolved magnetoresistance. The Fermi surface of UPt_3 is one of the most distinct and thoroughly studied of its kind, and observing any changes once confinement occurs would be of great interest.

Should superconductivity persist below this thickness limit, observation of an anomalous thermal Hall conductivity, k_{xy}, could also provide the evidence of the nodal structure of the order parameter inherent to the superconducting nature of the B-phase [40]. Finally, UPt_3 exhibits a non-trivial topology wherein its superconductive pairs have non-zero angular momentum, potentially granting the material with Majorana surface states [41]. Should a device be made where one could manipulate these Majorana states, their non-Abelian nature could be tested, providing major insight into the world of particle physics beyond the fermion-boson dichotomy [42].

Chapter 5

References

1. K. S. Novoselov, A. K. Geim, S. V. Morozov, D. Jiang, Y. Zhang, S. V. Dubonos, I. V. Grigorieva and A. A. Firsov, Science Mag. 306, 666-669 (2004)
2. V. Tayari, N. Hemsworth, I. Fakih, A. Favron, E. Gaufrès, G. Gervais, R. Martel and T. Szkopek, Nat. Comm. 6, 7702 (2015)
3. G. R. Stewart, Z. Fisk, J. O. Willis, and J. L. Smith, Phys. Rev. Lett. 52, 679 (1984)
4. R. Joynt and L. Taillefer, Rev. Mod. Phys. 74 (2002)
5. W. J. Gannon, W. P. Halperin, M. R. Eskildsen, P. Dai, U. B. Hansen, K. Lefmann and A. Stunault, Phys. Rev. B 96, 041111(R) (2017)
6. G. J. McMullan, P. M. C. Rourke, M. R. Norman, A. D. Huxley, N. Doiron-Leyraud, J. Flouquet, G. G. Lonzarich, A. McCollam and S. R. Julian, New J. Phys. 10 (2008)
7. W.-D. Schneider and C. Laubschat, Phys. Rev. B 23, 3 (1981)
8. B. Lussier, B. Ellman, and L. Taillefer, Phys. Rev. Lett. 73, 24 (1994)
9. P. Misra, *Handbook of Metal Physics* 2 (2007)
10. M. R. Norman and P. J. Hirschfeld, Phys. Rev. B 53, 9 (1996)
11. L. Taillefer, R. Newbury, G. G. Lonzarich, Z. Fisk and J. L. Smith, J. Mag. & Mag. Mat. 63-64, 372-376 (1987)
12. L. Taillefer and G. G. Lonzarich, Phys. Rev. Lett. 60, 15 (1988)
13. Julian, S. R., G. J. McMullan, N. Dorion-Leyraud, A. D. Huxley, M. P. Ray, M. R. Norman, J. Floquet, and G. G. Lonzarich, *The Fermi Surface of UPt3* University of Cambridge, Cambridge (2000)
14. N. Kimura, R. Settai, Y. Onuki, H. Toshima, E. Yamamoto, K. Maezawa, H. Aoki and H. Harima, J. Phys. Soc. Jpn. 64, 3881-3889 (1995)

15. T. Ito, H. Kumigashira, Hyeong-Do Kim, T. Takahashi, N. Kimura, Y. Haga, E. Yamamoto, Y. Onuki and H. Harima, Phys. Rev. B 59, 13 (1999)
16. A. Ashrafi, E. I. Rashba and D. L. Maslov, Phys. Rev. B 88, 075115 (2013)
17. S. L. Cooper, M. V. Klein, Z. Fisk and J. L. Smith, Phys. Rev. B 37, 4 (1988)
18. R. A. Fisher, S. Kim, B. F. Woodfield, N. E. Phillips, L. Taillefer, K. Hasselbach, J. Flouquet, A. L. Giorgi and J. L. Smith, Phys. Rev. Lett. 62, 12 (1989)
19. J. Flouquet, J.P. Brison, K. Hasselbach, L. Taillefer , K. Behnia, D. Jaccard and A. de Visser, Physica C 185-189, 372-378 (1991)
20. K. Hasselbach, L. Taillefer, and J. Flouquet, Phys. Rev. Lett. 63, 1 (1989)
21. L. Taillefer, F. Piquemal and J. Flouquet, Physica C 153-155, 451-452 (1988)
22. A. Schenstrom, M-F. Xu, Y. Hong, D. Bein, M. Levy, B. K. Sarma, S. Adenwalla, Z. Zhao, T. Tokuyasu, D. W. Hess, J. B. Ketterson, J. A. Sauls, and D. G. Hinks, Phys. Rev. Lett. 62, 332 (1989)
23. K. Behnia, L. Taillefer, J. Flouquet, D. Jaccard, K. Maki, Z. Fisk, J. Low Temp. Phys. 84 (1991)
24. N. Keller, J. P. Brison, P. Lejay, J. L. Tholence, A. Huxley, L. Schmidt, A. Buzdin, J. Flouquet, Physica B 206 & 207, 568-573 (1995)
25. H. v. Löhneysen, Physica B 197, 551-562 (1994)
26. K. A. Gschneidner, J.-C. G. Bünzli and V. K. Pecharsky, *Handbook on the Physics and Chemistry of Rare Earths* 34 (2004)
27. T. Trappmann, H. v. Löhneysen and L. Taillefer, Phys. Rev. B 43, 16 (1991)
28. S. M. Hayden, L. Taillefer, C. Vettier and J. Flouquet, Phys. Rev. Lett. B 46, 13 (1992)
29. B. Lussier, B. Ellman and L. Taillefer, Phys. Rev. B 53, 9 (1996)
30. M. J. Graf, S.-K. Yip and J. A. Sauls, J. Low Temp. Phys. 102 (1996)
31. H. Tou, Y. Kitaoka, K. Ishida, K. Asayama, N. Kimura, Y. Onuki, E. Yamamoto, Y. Haga, and K. Maezawa, Phys. Rev. Lett. 80, 14 (1998)
32. Y. Tsutsumi, K. Machida, T. Ohmi and M. Ozaki, J. Phys. Soc. Jpn. 81 (2012)
33. G. M. Luke, A. Keren, L. P. Le, W. D. Wu, Y. J. Uemura, D. A. Bonn, L. Taillefer and J. D. Garrett, Phys. Rev. Lett. 71, 9 (1993)
34. E. R. Schemm, W. J. Gannon, C. M. Wishne, W. P. Halperin and A. Kapitulnik, Science Mag. 345 (2014)

35. W. J. Gannon, W. P. Halperin, C. Rastovski, K. J. Schlesinger, J. Hlevyack, M. R. Eskildsen, A. B. Vorontsov, J. Gavilano, U. Gasser and G. Nagy, New J. Phys. 17 (2015)
36. J. D. Strand, D. J. Van Harlingen, J. B. Kycia and W. P. Halperin, Phys. Rev. Lett. 103, 197002 (2009)
37. P. A. Temple and C. E. Hathaway, Phys. Rev. B 7, 8 (1973)
38. P. Borowicz, M. Latek, W. Rzodkiewicz, A. Laszcz, A. Czerwinski and J. Ratajczak, Adv. Nat. Sci.: Nanosci. Nanotechnol. 3 (2012)
39. H. Wang, X. Huang, J. Lin, J. Cui, Y. Chen, C. Zhu, F. Liu, Q. Zeng, J. Zhou, P. Yu, X. Wang, H. He, S. H. Tsang, W. Gao, K. Suenaga, F. Ma, C. Yang, L. Lu, T. Yu, E. H. T. Teo, G. Liu and Z. Liu, Nat. Comm. 8, 394 (2017)
40. P. Goswami and A. H. Nevidomskyy, Phys. Rev. B 92, 214504 (2015)
41. Y. Yanase and K. Shiozaki, Phys. Rev. B 95, 224514 (2017)
42. A. Stern, Nature 464, 187-193 (2010)